Pyrolysis of Conductive 2D Coordination Polymers for Use as Solid Acid Fuel Cell Electrode Materials

J. August Ridenour[1], William A. Maza[1], Olga Baturina[1], Bethany Hudak[2], Hannah Ashberry[3], Brian L. Chaloux[1], Matthew T. Finn[1], Albert Epshteyn[1]

[1] Chemistry Division, US Naval Research Lab, 4555 Overlook Ave, SW, Washington, D.C., 20375

[2] Materials Science and Technology Division. US Naval Research Laboratory, 4555 Overlook Ave, SW, Washington, D.C., 20375

[3] Former NRC Postdoctoral Fellow, Chemistry Division, US Naval Research Lab, 4555 Overlook Ave, SW, Washington, D.C. 20375

Abstract

There is continued interest in the development of next-generation hydrogen-based energy systems that have greater power output, energy density, reliability, and lower costs. Solid acid fuel cells (SAFCs), which use solid acid electrolyte membranes and operate at intermediate temperatures (150–450 ºC), have the potential to address those technological targets.[1, 2] However, due to challenges arising from having a solid electrolyte, SAFC electrodes underperform as compared to those used for polymer electrolyte fuel cells (PEMFCs), and development of new materials is needed to tackle challenges associated with producing high electrochemically active surface area (ECSA) electrodes for solid-state architectures in SAFCs. Based on the requisite desirable properties, metal-organic coordination polymers[3] are attractive precursor compounds for producing new SAFC electrode materials; specifically due to existing porosity for gas diffusion, catalytically-active metal nodes, and a tunable carbon framework that can be made to become more electrically conductive via pyrolysis. Here we investigate metal-organic hybrid precursor materials modified *via* pyrolysis under vacuum to create metal-doped graphitized materials in pursuit of highly electrically conductive and porous carbonaceous materials with embedded metal nanoparticles. We submit these results as an important step toward producing more robust SAFC electrode materials.

Introduction

Intermediate temperature fuel cell technologies which enable operation in the temperature range of 100–450 °C offer the possibility of improvements over other fuel cell systems, such as polymer electrolyte fuel cells (PEMFCs), or solid oxide fuel cells (SOFCs).[4, 5] Higher operational temperatures as compared to PEMFCs can provide multiple fuel cell system benefits including improved water management, heat rejection, and possibly provide additional benefits such as ability to use non-precious metal catalysts, as well as reducing catalyst susceptibility to poisoning. Bulky humidification systems may be eliminated with improved proton mobility kinetics, alternative proton mobility pathways (*i.e.* non-water), and elimination of need for active humidification.[6, 7] Further, intermediate temperature systems operating in the 100-450 °C range can be constructed from standard engineering materials without the use of expensive refractory components.[6, 8, 9] One type of intermediate temperature fuel cell systems, solid acid fuel cells (SAFCs), utilize a highly protonated solid-form acid as the electrolyte membrane.[1, 2] Due to the lack of liquid/gel proton electrolytes in these systems, SAFC electrodes suffer from lower electrochemical surface area and therefore lower power output. New approaches in nanoscopically textured/architected electrode design are needed to produce higher electrochemically active surface areas (ECSAs) for SAFC-specific requirements stemming from electrolyte compatibility considerations.

The fundamental requirements of viable electrode materials include reasonable electrical conductivity, porosity for gas infiltration, maximized number of accessible catalytic sites, and stability under fuel cell operating conditions; yet materials that exhibit all characteristics at appropriate levels for SAFC operation are few and noteworthy.[12-14] Metal-organic-based hybrid materials, particularly those with multi-dimensional architectures, may fill many of these attribute niches.[15, 16] Pyrolytic post-modification of such hybrid precursors can then improve chemical and thermal stability, as well as electrical conductivity, through graphitization of organics to access beneficial architectures and/or generate catalytic sites.[17-19] As such, we have investigated the modification of the highly conductive metal-hexaaminotriphenylene (HATP) coordination polymers[20, 21] toward performance improvement *via* post-synthetic pyrolysis. Initial investigations found that anaerobic thermal decomposition of Ni_3HATP_2 produces nanoparticles (NPs), with modest size control afforded by pyrolysis temperature while confined in a C-based matrix. In search of a more appropriate electrode

material, a novel Pt-HATP precursor was synthesized using methodology similar to that of Ni_3HATP_2, yet producing a significantly different crystalline material. Pyrolysis experiments with the Pt-HATP demonstrated similar reductive decomposition accompanied by graphitization of the organic linkers and the formation of size-controllable Pt NPs with significantly greater size control over the Ni system. Electrochemical experiments to investigate the Pt-HATP activity for ORR catalysis using rotating disk electrode (RDE) methods are presented.

Synthesis, Pyrolysis, and Characterization

All precursor materials discussed herein were synthesized in a process modified from the original $Ni_3(HITP)_2$ investigation by Dincă, *et al*.[20, 21] A metal salt and the 2,3,6,7,10,11-hexaaminetriphenylene (HATP) ligand were combined in an aqueous ammonia solution and left stirring overnight while heated to 65 °C. A black solid suspension was then filtered, washed, and dried. This black solid, as the metal-organic precursor material, was then pyrolyzed at 600 °C in a tube furnace at 50 mtorr under dynamic vacuum.

High angle annular dark field (HAADF) imaging and *in situ* pyrolysis were done to investigate the pyrolytic formation of nanoparticles with a scanning transmission electron microscope (Nion UltraSTEM-X 200 STEM, 60 kV, 10^{-9} Torr) equipped with a Protochips E-chip heating TEM grid. Samples were drop-cast with EtOH onto the grid, fully dried, and upon insertion into the instrument heated *in situ* to 500 °C in 50 °C steps and from 500 °C to 1200 °C in 100 °C steps, with a nearly instantaneous rate of heating at 1000 °C/ms. Thermogravimetric analysis and differential scanning calorimetry (TGA/DSC) were conducted on both the Ni-HATP and the Pt-HATP materials to investigate inert atmosphere thermal decomposition.

For electrochemical analyses, an ink was prepared by dispersing 8 mg of the pyrolyzed catalyst in 2 mL of inking solution (20 mL of H_2O, 80 mL of IPA, and 0.4 mL of 5 wt. % Nafion ionomer solution (Ion Power, Liquion 1100)). The catalyst suspension was homogenized by ultrasound, stirred overnight, then sonicated again prior to drop-casting 10 and 20 µL droplets on the surface of a 5 mm mirror-polished and clean glassy carbon electrode. The same procedure was used for both the 40 wt. % Pt/VC and the 38 wt. % Pt nanoparticles embedded in the pyrolyzed Pt-HATP material, respectively. Cyclic voltammetry (CV) and polarization curves were collected in a 125 mL commercial 3-electrode electrochemical cell filled with 0.1 M $HClO_4$ solution, using a Autolab µ-III potentiostat (Metrohm). Spiral Pt wire and Ag/AgCl served as a counter and reference electrodes, respectively. The electrolyte solution was purged with UHP N_2 or O_2 prior to collecting CV and polarization curves, and bubbling was maintained throughout the electrochemical measurements. Prior to collecting polarization curves, the catalyst was activated by running 120 CV curves at 200 mV s^{-1} between -0.35 and 1.15 V. The ECSAs were calculated from hydrogen desorption regions on CV curves as described previously[22] and kinetic currents were extracted from total ORR currents using a previously reported and established procedure.[22]

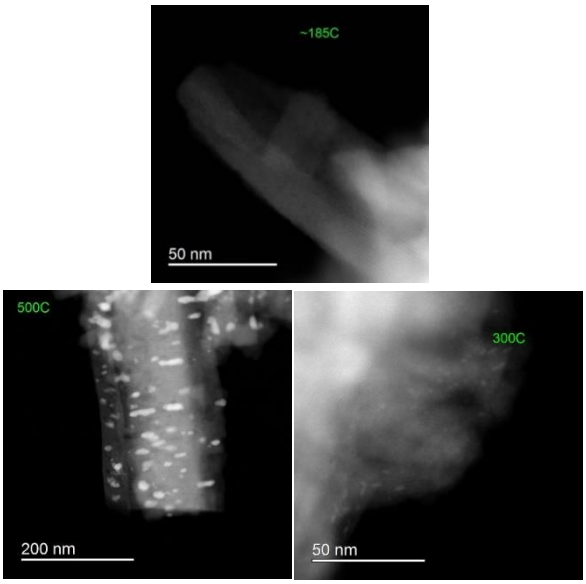

Figure 1. HAADF images of $Ni_3(HITP)_2$. Left) Crystalline domains show 1.8 nm pores. Middle) In regions of high crystallinity, thermal decomposition facilitates formation of rod-shaped Ni nanoparticles along the pores of the coordination polymer. Right) Elongated nickel nanoparticles grow as the temperature increases.

Discussion

As its most fundamental function, a fuel cell electrode must be sufficiently electrically conductive. Our search for suitable SAFC electrode materials began with the metal-organic coordination polymer, $M_3(HATP)_2$, known for high intrinsic bulk electrical conductivity, as reported by Dincă, *et al*.[20] Unmodified $M_3(HATP)_2$ (where M = Ni^2, Cu^{2+}, or Co^{2+}) materials have been shown to exhibit conductivities comparable to common amorphous carbon substrates (1 to 10 S/cm^{-1} range) and some were also found to exhibit significant internal surface areas (*e.g.* ~281.0 m^2/g for $Co_3(HATP)_2$).[23] This

transition metal-HATP material system provides an attractive starting point to further improve conductivity and stability of the proposed electrode material *via* pyrolysis.

To facilitate the synthesis and characterization of our proposed Pt-HATP material, the previously reported $Ni_3(HATP)_2$ [20, 24] was synthesized as confirmed *via* HAADF-TEM imaging (**Fig. 1**). Rod-like crystalline domains of $Ni_3(HATP)_2$ show pore sizes on par with published data (~1.8 nm).[21] Heating this material to 300 °C during TEM imaging forms Ni NPs smaller than 5 nm (**Fig. 1**). Interestingly, in regions of high crystallinity, elongated rod-like Ni NPs are formed along the pores of the coordination polymer, providing a proxy visualization of the original material pore structure. As treatment temperatures are increased, further NP growth occurs yielding Ni particles of lengths between 5 and 25 nm.

The Pt-HATP precursor synthesis was conducted under similar conditions as for $Ni_3(HATP)_2$, although the dark brown solid product is of an unknown structure. Pt-HATP behaves

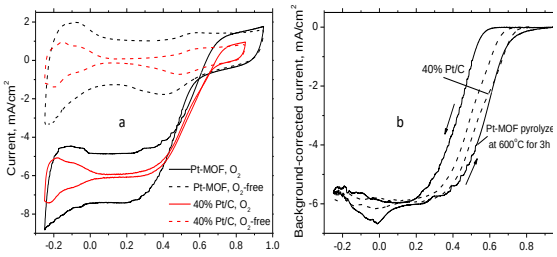

Figure 3. (a) CV and ORR polarization curves of thin films of 38 wt% Pt-HATP and 40 wt% Pt/C catalysts (0.1M $HClO_4$, 20 mV/s, 1600 rpm); (b) ORR corrected for current in O_2-free environment. Pt loading: 153.2 and 81.6 $\mu g_{Pt}/cm^2$ for Pt-HATP and Pt/C, respectively.

similarly during pyrolysis, with decomposition at the same temperature. Spheroidal Pt NPs of sizes significantly smaller than 5 nm are observed at 300 °C and grow to 3-5 nm by 500 °C (**Fig. 2**). Pt NP distribution *density* varies significantly, although the Pt NP *size* distribution is narrow at specific pyrolysis temperatures (**Fig. 2**). This likely stems from a much more stable structure of the material that likely is the result of tetrahedral binding around the Pt, as opposed to the square planar arrangement for the Ni structure; although at this point this is just conjecture. Unlike the $Ni_3(HATP)_3$ material, the Pt NPs in the pyrolyzed material are crystalline, remain small over a wide temperature range (**Fig. 2**), and only grow to sizes larger than 25 nm above 1000 °C.

Bulk precursor Pt-HATP pyrolyzed '*ex situ*' in a tube furnace under vacuum shows similar Pt NP growth, according to HAADF imaging. Homogenously sized spherical NPs form at 300 °C, and continue growing as temperature increases, as shown by evidence of NP ripening within the 300 °C to 600 °C temperature range (**Fig. 2**).

CV and polarization curves (**Fig. 3**) were measured on thin films of the 38 wt. % Pt-HATP sample that had been pyrolyzed at 300 °C and a 40 wt. % Pt/C standard. Both CV curves have well-pronounced hydrogen (-0.25 <E< 0.08V) and oxygen adsorption/desorption regions. The hydrogen region is featureless for Pt-HATP as compared to Pt/VC, possibly due to smaller sized Pt NPs (2.5 nm vs 5 nm for Pt/C). When comparing the Pt-HATP sample versus the Pt/C control, the adsorption of OH groups from water activation occurs at the same potential of *ca* 0.55V, while the reduction of surface

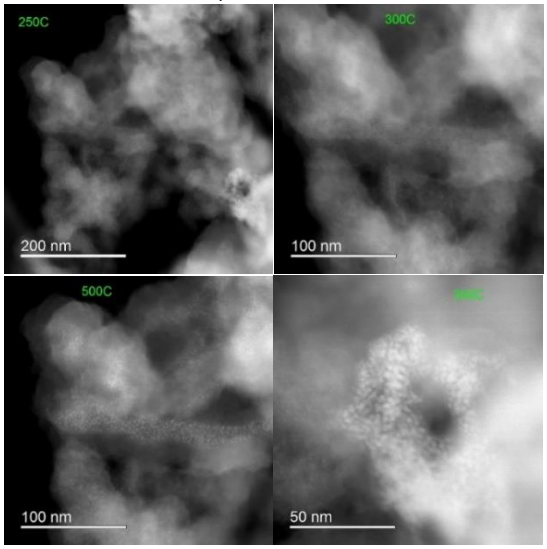

Figure 2. HAADF images of Pt-HATP at several temperatures showing evolution of Pt NP during *in situ* pyrolysis. Top. left) 250 °C; Top. right) 300 °C, decomposition temperature, Pt NPs begin to form; Bot. left) 500 °C; Bot. right) Area of high Pt NP density.

oxide occurs at a more negative potential of 0.4V for Pt-HATP compared to 0.5V for Pt/C; again possibly due to the smaller size of Pt. Interestingly, the Pt-HATP CV curve has higher currents in the double layer region, located between hydrogen and oxygen adsorption/desorption regions, which are attributed to electrical double layer charging currents, leading to distortion of the ORR polarization curves. The ORR curves (**Fig. 3**) have a plateau at -6 mA/cm^2 in the diffusion-limited region for the Pt/C catalyst corresponding to a $4e^-$ ORR pathway. At potentials more negative than 0.06V, however, the plateau is affected by currents in the hydrogen

adsorption/desorption region and is even more pronounced for the Pt-HATP catalyst. In the region occurring under mixed kinetic-diffusion control (0.3 V<E<0.68 V), ORR currents on Pt/C catalyst are more negative than those on Pt-HATP at a given potential, which may indicate higher activity of Pt-HATP. Considering the high contribution of capacitive currents into the ORR currents for Pt-HATP catalysts, we calculated ORR currents corrected for the currents measured in O_2-free environment (**Fig. 3**). Both polarization curves have a more traditional shape, with clearly separated cathodic and anodic scans. In the diffusion-limited region, both are centered around -6 mA/cm^2, which indicates a 4 e- pathway for both catalysts (rotation rate; 1600 rpm). In the mixed kinetic-diffusion region, the hysteresis between the cathodic and anodic sweeps is more pronounced for Pt-HATP, which agrees with higher capacitive currents observed for this catalyst. To compare area- and mass-specific activities of the two catalysts, the ECSAs and kinetic currents were calculated at a potential of 0.65 V. The results are presented in **Table 1**. Unexpectedly, the ECSA for the Pt-HATP catalyst is more than a factor of 2 lower than that of commercial Pt/C. One possible reason for that may be lower utilization of 2.5 nm Pt NPs in the framework due to incomplete electrical connectivity with all Pt NPs, or porosity occlusions. The area-specific activities are close, indicating that there is potential for improvement of the Pt-HATP catalyst.

Table 1. ECSA, area- and mass-specific activities for Pt-HATP and Pt/C for ORR at 0.65V in 0.1M $HClO_4$: 20

	Pt load, $\mu g_{Pt}/cm^2$	Specific activity, Mass - A/mg_{Pt}
38 wt% Pt-HATP	153.2	0.011
40 wt% Pt/C	81.6	0.022
	ECSA, m^2/g_{Pt}	Specific activity, Area - $\mu A/cm^2_{Pt}$
38 wt% Pt-HATP	22.0	48.6
40 wt% Pt/C	49.8	45

Conclusions

In situ in vacuo pyrolysis in TEM captures the appearance of small Pt NPs (2 to 5 nm) at low temperatures and provides a mechanistic link between thermal degradation of the amine of the HATP ligand and reduction of coordinated Pt^{2+}. Ripening occurs as the pyrolysis temperature increases, providing a range of Pt NPs sizes from 2 nm to several hundred. The pyrolyzed Pt-HATP material represents an interesting pyrolytic approach to generating size-controlled platinum nanoparticles within a carbonized framework. This method produces materials with modest ORR activity in acidic media, with potential for future engineered improvements. Ultimately, this novel Pt-HATP electrocatalyst demonstrates promising ORR activity, yet greater Pt utilization is needed to improve overall performance. Efforts to increase effective catalytic surface area are currently underway, as are experiments utilizing pyrolyzed Pt-HATP as an electrode in a PEM fuel cell.

References

1. Haile, S. M.; Chisholm, C. R. I.; Sasaki, K.; Boysen, D. A.; Uda, T., *Faraday Discussions* **2007,** *134*, 17-34.
2. Boysen, D. A.; Uda, T.; Chisholm, C. R. I.; Haile, S. M., *Science* **2004,** *303*, 68-70.
3. Xie, L. S.; Skorupskii, G.; Dinca, M., *Chem. Rev.* **2020,** *120* (16), 8536-8580.
4. Lee, S.-Y.; Ogawa, A.; Kanno, M.; Nakamoto, H.; Tasuda, T.; Watanabe, M., *J. Am. Chem. Soc.* **2010,** *132*, 9764-9773.
5. Azad, A. K.; Abdalla, A. M.; Afif, A.; Azad, A.; Afroze, S.; Idris, A. C.; Park, J.-Y.; Saqib, M.; Radenahmad, N.; Hossain, S.; Elius, I. B.; Al-Mamun, M.; Zaini, J.; Al-Hinai, A.; Reza, M. S.; Irvine, J. T. S., *Scientific Reports* **2021,** *11* (1), 19382.
6. Ward, M. D.; Chaloux, B. L.; Johannes, M. D.; Epshteyn, A., *Adv. Mater.* **2020,** *32* (42), 2003667.
7. Chaloux, B. L.; Ridenour, J. A.; Johannes, M. D.; Epshteyn, A., *Adv. Energy Sustainibility Res.* **2022,** *3*, 2200029.
8. Ormerod, R. M., *Chem. Soc. Rev.* **2003,** *32*, 17-28.
9. Haile, S. M., *MaterialsToday* **2003,** *6* (3), 24-29.
10. Baturina, O. A.; Aubuchon, S. R.; Wynne, K. J., *Chem. Mater.* **2006,** *18* (6), 1498-1504.
11. Joo, S. H.; Park, J. Y.; Tsung, C.-K.; Yamada, Y.; Yang, P.; Somorjai, G. A., *Nature Materials* **2009,** *8*, 126-131.
12. Uda, T.; Haile, S. M., *Electrochem. Solid-State Lett.* **2005,** *8* (5), A245-A246.
13. Varga, A.; Brunelli, N. A.; Louie, M. W.; Giapis, K. P.; Haile, S. H., *J. Mater. Chem.* **2010,** *20* (30), 6309-6315.
14. Papandrew, A. B.; Crisholm, C. R. I.; Elgammal, R. A.; Özer, M. M.; Zecevic, S. K., *Chem. Mater.* **2011,** *23* (7), 1659-1667.
15. Zheng, W.; Lee, L. Y. S., *ACS Energy LEtt* **2021,** *6* (8), 2838-2843.
16. Sulaiman, M. R.; Gupta, R. K., In *Nanotechnology in Fuel Cells*, Song, H.; Nguyen, T. A.; Yasin, G., Eds. Elsevier Inc.: 2022; pp 173-199.
17. Wang, Y.; Wang, J.; Wei, D.; Li, M., *ACS Appl. Mater. Interfaces* **2019,** *11* (39), 35755-35763.
18. Mukherjee, S.; Hou, S.; Watzele, S. A.; Garlyyev, B.; Li, W.; Bandarenka, A. S.; Fischer, R. A., *ChemElectroChem* **2021,** *9* (7), e202101476.
19. Zou, L.; Hou, C.-C.; Liu, Z.; Pang, H.; Xu, Q., *J. Am. Chem. Soc.* **2018,** *140* (45), 15393-15401.
20. Sheberla, D.; Sun, L.; Blood-Forsythe, M. A.; Er, S.; Wade, C. R.; Brozek, C. K.; Aspuru-Guzik, A.; Dincă, M., High *J. Am. Chem. Soc.* **2014,** *136* (25), 8859-8862.
21. Chen, T.; Dou, J.-H.; L, Y.; Sun, C.; Libretto, N. J.; Skorupskii, G.; Miller, J. T.; Dincă, M., *J. Am. Chem. Soc.* **2020,** *142* (28), 12367-12373.
22. Baturina, O. A.; Garsany, Y.; Zega, T. J.; Stroud, R. M.; Schull, T.; Swider-Lyons, K. E., *J. Electrochem. Soc.* **2008,** *155* (12), B1314-B1321.
23. Xing, D.; Wang, Y.; Zhou, P.; Liu, Y.; Wang, Z.; Wang, P.; Zheng, Z.; Cheng, H.; Dai, Y.; Huang, B., *Applied Catalysis B: Environmental* **2020,** *278*, 119295.
24. Miner, E. M.; Fukushima, T.; Sheberla, D.; Sun, L.; Surendranath, Y.; Dincă, M., *Nature Communications* **2016,** *7*, 10942.